

# Climatology of the planetary boundary layer over the continental United States and Europe

Dian J. Seidel,<sup>1</sup> Yehui Zhang,<sup>2</sup> Anton Beljaars,<sup>3</sup> Jean-Christophe Golaz,<sup>4</sup>  
Andrew R. Jacobson,<sup>5</sup> and Brian Medeiros<sup>6</sup>

Received 20 May 2012; accepted 19 June 2012; published 6 September 2012.

[1] Although boundary layer processes are important in climate, weather and air quality, boundary layer climatology has received little attention, partly for lack of observational data sets. We analyze boundary layer climatology over Europe and the continental U.S. using a measure of boundary layer height based on the bulk Richardson number. Seasonal and diurnal variations during 1981–2005 are estimated from radiosonde observations, a reanalysis that assimilates observations, and two contemporary climate models that do not. Data limitations in vertical profiles introduce height uncertainties that can exceed 50% for shallow boundary layers (<1 km) but are generally <20% for deeper boundary layers. Climatological heights are typically <1 km during daytime and <0.5 km at night over both regions. Seasonal patterns for daytime and nighttime differ; daytime heights are larger in summer than winter, but nighttime heights are larger in winter. The four data sets show similar patterns of spatial and seasonal variability but with biases that vary spatially, seasonally, and diurnally. Compared with radiosonde observations, the reanalysis and the climate models produce deeper layers due to difficulty simulating stable conditions. The higher-time-resolution reanalysis reveals the diurnal cycle in height, with maxima in the afternoon, and with amplitudes that vary seasonally (larger in summer) and regionally (larger over western U.S. and southern Europe). The lower-time-resolution radiosonde data and climate model simulations capture diurnal variations better over Europe than over the U.S., due to differences in local sampling times.

**Citation:** Seidel, D. J., Y. Zhang, A. Beljaars, J.-C. Golaz, A. R. Jacobson, and B. Medeiros (2012), Climatology of the planetary boundary layer over the continental United States and Europe, *J. Geophys. Res.*, 117, D17106, doi:10.1029/2012JD018143.

## 1. Introduction

[2] Understanding and predicting weather, climate, and air quality depend on reasonably accurate characterization of vertical exchange of heat, moisture, carbon dioxide and other greenhouse gases, dust and other aerosols, and air pollutants between the Earth's surface and the free atmosphere through the planetary boundary layer (PBL). The convective and turbulent processes controlling mixing are complex, nonlinear, and chaotic, and they vary on a wide range of space and time scales. Air pollution and PBL

studies often employ the concept of mixing height to characterize these processes. *Seibert et al.* [2000] present a particularly instructive and comprehensive review of the topic and describe many approaches to evaluating mixing height and complexities in their application. Discussion of mixing height or other measures of PBL height is much less common in the climatological literature, which we attribute to two factors. First, although PBL processes in climate models are parameterized, many schemes explicitly model some form of PBL height, yet they have rarely been evaluated (with the notable exception of *Holtstlag and Boville* [1993]). Second, there are no climatological (large space and time scale) observational analyses of the PBL, mainly because of the lack of direct measurements of PBL height and of suitable measurements that could be used to estimate it [*Liu and Liang*, 2010].

[3] This latter problem may be partially remedied through analysis of new data sources, including observations by ceilometer [*Eresmaa et al.*, 2006; *van der Kamp and McKendry*, 2010], lidar [*Hennemuth and Lammert*, 2006; *Tucker et al.*, 2009], wind-profiling and boundary layer radar [*Angevine et al.*, 1994; *Bianco and Wilczak*, 2002] and sodar [*Beyrich*, 1997; *Lokoshchenko*, 2002]. Other types of observations, including radio occultation measurements from global navigational satellite systems [*Ratnam and*

<sup>1</sup>Air Resources Laboratory, NOAA, Silver Spring, Maryland, USA.

<sup>2</sup>Applied Hydrometeorological Research Institute, Nanjing University of Information Science and Technology, Nanjing, China.

<sup>3</sup>European Centre for Medium-Range Weather Forecasting, Reading, UK.

<sup>4</sup>Geophysical Fluid Dynamics Laboratory, NOAA, Princeton, New Jersey, USA.

<sup>5</sup>University of Colorado at Boulder and NOAA Earth System Research Laboratory, Boulder, Colorado, USA.

<sup>6</sup>National Center for Atmospheric Research, Boulder, Colorado, USA.

Corresponding author: D. J. Seidel, Air Resources Laboratory, NOAA, 1315 East-West Hwy., Silver Spring, MD 20910, USA. (dian.seidel@noaa.gov)

Basha, 2010; Guo et al., 2011, C. O. Ao et al., Planetary boundary layer heights from GPS radio occultation refractivity and humidity profiles, submitted to *Journal of Geophysical Research*, 2012], and aerosol observations from satellites [Jordan et al., 2010; McGrath-Spangler and Denning, 2012] have been used to estimate various PBL height metrics. Depending on the atmospheric parameter measured and observational uncertainties, different types of observations may reveal different aspects of PBL structure. Moreover, application of different methods of determining PBL height to a single data set can yield a wide range of results [Seibert et al., 2000; Seidel et al., 2010; Beyrich and Leps, 2012], which underscores the importance of applying consistent algorithms to consistent types of atmospheric profile information when comparing PBL heights from different locations and times.

[4] Using a consistent method and a traditional data source, radiosonde observations, this study presents PBL climatologies. Previous studies of this ilk include the pioneering research of Holzworth [1964, 1967] who used early radiosonde data to study mixing height climatology over the U.S., and the U.S. Environmental Protection Agency Air Quality Modeling Group's U.S. mixing height data product (available at <http://www.epa.gov/scram001/mixingheightdata.htm>) that covers mainly the decade of the 1980s. To our knowledge, neither of these studies has been updated, nor do comparable climatologies exist for other countries, although climatologies may exist for specific locations (such as Lindenberg, Germany [Beyrich and Leps, 2012]). This paper presents new climatologies for the U.S. and Europe based on long-term radiosonde observations and compares the radiosonde climatology with PBL representations in a modern reanalysis data product and in two contemporary climate models, which has not been attempted previously.

## 2. Radiosonde, Reanalysis and Climate Model Data

[5] Our analysis is based on radiosonde observations, the most recent reanalysis of the European Centre for Medium-Range Weather Forecasting (ERA-Interim) [Dee et al., 2011], and simulations by two state-of-the-art climate models. Climatological statistics are derived from twice-daily (0000 and 1200 UTC) sampling of these data sets over the 25-year period 1981–2005 within two midlatitude spatial domains: the continental United States ( $\sim 25\text{--}50^\circ\text{N}$ ,  $65\text{--}125^\circ\text{W}$ ) and Europe (including a small region of North Africa on the Mediterranean coast but referred to here as Europe,  $\sim 35\text{--}60^\circ\text{N}$ ,  $10^\circ\text{W}\text{--}30^\circ\text{E}$ ). These regions were selected because they are better sampled by the radiosonde network than other midlatitude areas and they are home to large populations with concerns about air quality. We deliberately avoided the Arctic regions (Alaska and northern Scandinavia), where the planetary boundary layer often exhibits surfaced-based inversions [Zhang et al., 2011], tropical regions (Hawaii and the southern and eastern Mediterranean region), which we expect would frequently experience deep convection and thus ill-defined PBL heights, and Asian and Southern Hemisphere midlatitude regions with sparser radiosonde networks.

[6] Radiosonde data are from two sources, the enhanced version of the Integrated Global Radiosonde Archive (IGRA) [Durre and Yin, 2008] maintained by the NOAA National Climatic Data Center and the more spatially and temporally limited (with 65 stations within the continental U.S. and none in Europe during 1998–2007), but higher vertical resolution radiosonde data archive maintained by the Stratospheric Processes and their Role in Climate Data Center (<http://www.sparc.sunysb.edu/html/hres.html>) [Wang and Geller, 2003]. The SPARC data were used to assess potential uncertainties in results from the more comprehensive IGRA data. IGRA data from 69 U.S. and 53 European stations met the following sampling requirements: at least 300 soundings per calendar month or per season during 1981–2005, all having at least 7 reported data levels between the surface and 500 hPa. On average, IGRA soundings from low-elevation ( $<500$  m) stations had 15 (typically 10 to 30) data levels, and corresponding soundings from the SPARC archive averaged more than 100 levels, within this lower tropospheric layer.

[7] The ERA-Interim [Dee et al., 2011] is a reanalysis data product based on the assimilation of multiple types of observational data, including radiosonde observations, into a numerical weather prediction model, with two important goals of optimizing the representation of the atmosphere and providing data in regions and at times without actual observations, both in a physically consistent manner. This assimilation data product complements the radiosonde data by providing complete spatial and temporal coverage at about  $0.7$  degrees latitude and longitude resolution and 3 h temporal resolution. ERA-Interim has 60 model levels in the vertical using hybrid coordinates that follow the terrain at the surface and gradually transition to pressure coordinates at the model top, 0.1 hPa. The boundary layer is fairly well resolved with the lowest model levels at about 10, 30, 60, 100, 160, and 240 m above the model surface. The level spacing increases gradually with height with a vertical resolution of about 200 m at 900 hPa and 500 m at 500 hPa. Data products, initially available at a more limited set of pressure levels at a lower horizontal resolution of 1.5 degrees, include boundary layer height estimates [European Center for Medium-Range Weather Forecasting, 2006]. We do not employ those estimates because they are computed using an algorithm that is not applicable to radiosonde data because turbulence parameters are required. For consistency, and to take advantage of the full resolution of ERA-Interim, the model level data were re-processed at the original resolution with the same algorithm that is applied to the radiosonde data. Without showing a comprehensive comparison, we note that the ERA-interim product (i.e., with the ECMWF algorithm) shows higher heights, especially over high elevation regions, than the algorithm used in this study. Differences are  $<100$  m at night and several 100 m during daytime, and they are larger over ocean than over land.

[8] Simulations from the NOAA Geophysical Fluid Dynamics Laboratory's Atmospheric Model 3 (GFDL AM3) [Donner et al., 2011] and from the National Center for Atmospheric Research Community Atmosphere Model version 5.0 (NCAR CAM5) [Neale et al., 2010] do not directly assimilate any atmospheric profile observations, and their representations of the planetary boundary layer are purely model-generated. The GFDL AM3 uses a cubed-sphere grid

with approximately  $2^\circ$  resolution, NCAR CAM5 uses horizontal grid spacing of  $0.9^\circ$  latitude  $\times$   $1.25^\circ$  longitude, and our analysis employs these resolutions. Approximate vertical resolutions between the surface and 500 hPa are 15 and 12 levels in AM3 and CAM5, respectively.

[9] Both climate models and the ERA-Interim were sampled at 0000 and 1200 UTC to match the radiosonde observation times. These times represent near-midnight and near-noon conditions in Europe, and near-dusk and near-dawn conditions over the U.S., with longitudinal and seasonal variations causing spatial and temporal variations in the sampling of the diurnal cycle. We also use the 3-hourly ERA-Interim data and 6-hourly climate model output to evaluate diurnal variations in greater detail.

### 3. Methodology for Estimating Climatological Boundary Layer Heights

#### 3.1. Definition

[10] The literature contains many methods for estimating PBL mixing height [Seibert *et al.*, 2000], and we evaluated ten to identify one most suitable for this study, using the following criteria. The method must be based on parameters measured by or derivable from radiosonde observations and available in the ERA-Interim and both climate models. The method must be a positive semi-definite function, i.e., height  $\geq 0$  for all realistic atmospheric profiles. And it should yield estimates that are not strongly dependent on small differences in profile conditions.

[11] We tested the Richardson number (Ri) methods of Joffe *et al.* [2001] and Eresmaa *et al.* [2006]; the gradient Ri methods of Garratt [1992], Seibert *et al.* [2000] and Zilitinkevich and Baklanov [2002]; the bulk Ri methods of Vogelezang and Holtslag [1996] and Seibert *et al.* [2000] based on work by Troen and Mahrt [1986]; the parcel methods of Holzworth [1964, 1967] and Seibert *et al.* [2000]; the height of a surface-based inversion or the first temperature or humidity discontinuity [Hanna, 1969; Yamada, 1979; Keder, 1999]; the base of an elevated inversion or height of a significant change in potential temperature [Dayan *et al.*, 1988; Seibert *et al.*, 2000]; and two methods based on potential temperature gradients [Heffler, 1980; Marsik *et al.*, 1995; Keder, 1999]. An earlier analysis [Seidel *et al.*, 2010] demonstrated that climatological heights based on Ri and the parcel method were substantially (several 100 m) lower than heights of elevated inversions or on maximum humidity, temperature, or potential temperature gradients, and they showed greater diurnal and seasonal variability.

[12] The best method for this climatological analysis of large data sets proved to be the bulk Ri method originally proposed by Vogelezang and Holtslag [1996], because it is suitable for both stable and convective boundary layers, identifies a nonnegative height in all cases, and is not strongly dependent on sounding vertical resolution. The Ri is the ratio of turbulence associated with buoyancy to that associated with mechanical shear, where

$$\text{Ri}(z) = \frac{(g/\theta_{vs})(\theta_{vz} - \theta_{vs})(z - z_s)}{(u_z - u_s)^2 + (v_z - v_s)^2 + (bu_*^2)}$$

and  $z$  is height and  $s$  denotes the surface,  $g$  is the acceleration of gravity,  $\theta_v$  is virtual potential temperature (excluding condensate loading),  $u$  and  $v$  are component wind speeds,  $b$  is a constant and  $u_*$  is the surface friction velocity. Since  $u_*$  is not known from radiosonde data, we set  $b = 0$  and thus ignore surface frictional effects, which are much smaller than the bulk shear terms in the denominator and is not significant in stable conditions [Vogelezang and Holtslag, 1996]. The lowest level  $z$  at which interpolated Ri crosses the critical value of 0.25,  $z(\text{Ri}_{0.25})$ , is the main PBL height metric used in our analysis.

[13] Because “surface” observations in radiosonde reports include temperature, pressure and humidity at the 2 m level but do not include winds, we compute Ri based on “surface” information at the 2 m level, with 2 m winds set to zero. For the models and reanalysis, thermodynamic variables at 2 m were obtained by vertical interpolation between the surface and the lowest model level (typically between 20 and 60 m), and winds were set to zero, for consistency with the radiosonde data.

[14] In summary, we estimate  $z(\text{Ri}_{0.25})$  using  $\theta_v$ ,  $u$ , and  $v$  profiles to compute the Ri profile, setting  $b = 0$ , taking surface values of  $u$  and  $v$  to be zero. Scanning the Ri profile upward from the surface (at 2 m), the first level with  $\text{Ri} \geq 0.25$  is identified, and linear interpolation between that level and the next lowest level provides an estimate of  $z(\text{Ri}_{0.25})$ . The presence or absence of low-level cloud does not enter the calculation.

[15] Figure 1 illustrates the method applied to a sample summertime sounding from Minneapolis. The observed temperature, humidity and wind profiles (left and middle) from a single sounding, separately archived by both IGRA and SPARC, are used to compute Ri profiles (right). The higher resolution SPARC data yield  $z(\text{Ri}_{0.25})$  at 1.615 km, and the IGRA data yield 1.579 km. In this instance, the different data sources yield similar but not identical  $z(\text{Ri}_{0.25})$ .

#### 3.2. Methodological Uncertainties

[16] To quantify uncertainties in  $z(\text{Ri}_{0.25})$  determined using this bulk Ri method, we computed  $z(\text{Ri}_{0.25})$  from 400,644 soundings in the SPARC archive for 1998–2008 and from paired IGRA soundings at the same times and locations. Four sources of uncertainty were assessed, and the results are summarized in Figure 2, where uncertainties are presented as function of  $z(\text{Ri}_{0.25})$  and expressed both in absolute terms (m) and as a percentage of  $z(\text{Ri}_{0.25})$ . Figure 2e shows the frequency distribution and cumulative frequency distribution of  $z(\text{Ri}_{0.25})$  at both 0000 and 1200 UTC, indicating that estimated  $z(\text{Ri}_{0.25}) < 1$  km in 60% of daytime observations and 95% of nighttime observations. Almost all  $z(\text{Ri}_{0.25})$  estimates are  $< 4$  km for these U.S. soundings.

[17] The first source of uncertainty is the use of critical  $\text{Ri} = 0.25$ . Figures 1 and 2a compare heights based on critical values of 0.25 and 0.30 [Vogelezang and Holtslag, 1996]. In the sample case (Figure 1)  $\text{Ri} = 0.30$  at 1.836 km, 14% higher than  $z(\text{Ri}_{0.25})$ . We expect consistently higher estimates with higher threshold Ri, as shown in Figure 2a, but the differences are small. The correlation  $r = 1.00$ ; the median and 75th percentile values of the absolute

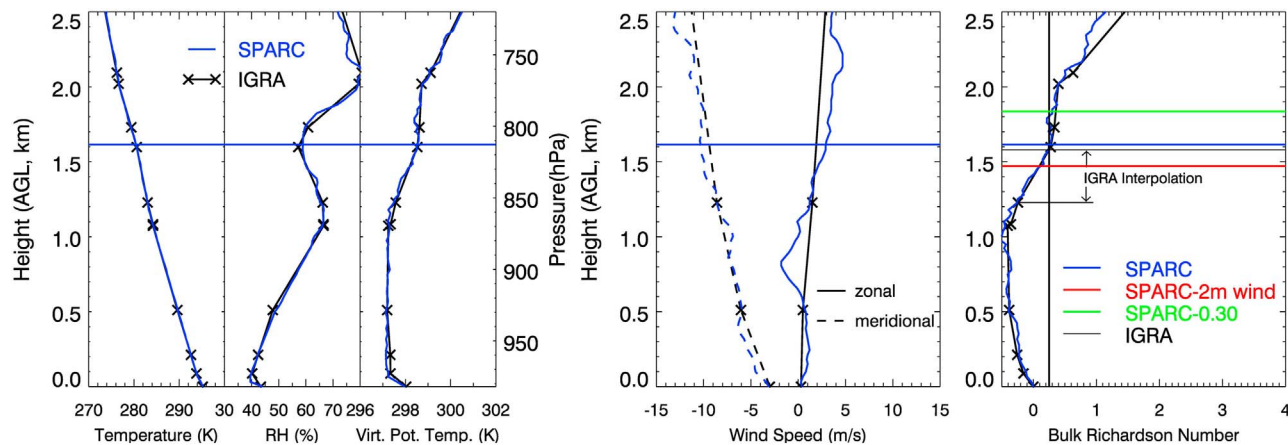


**Figure 1.** Vertical profiles of (left) temperature, relative humidity, and virtual potential temperature, (middle) wind speed, and (right) bulk Richardson number based on the 0000 UTC 28 June 2006 radiosonde observation at Minneapolis, Minnesota, USA ( $45^{\circ}\text{N}$ ,  $94^{\circ}\text{W}$ ) from the IGRA and SPARC data archives. IGRA data levels are shown with x, and the higher-resolution SPARC profiles are shown as continuous lines. Horizontal lines in Figure 1 (right) indicate boundary layer heights computed from both sets of profiles (SPARC and IGRA) using the method employed in this study and using slightly different methods (SPARC-2m wind and SPARC-0.3), as described in the text, to estimate methodological uncertainties.

uncertainties are  $<50$  m and  $<80$  m, respectively; the median and 75th percentile values of the associated relative uncertainties are both  $<5\%$  for  $z(\text{Ri}_{0.25}) > 2$  km, and  $<20\%$  for  $z(\text{Ri}_{0.25}) < 2$  km. This source of uncertainty is the smallest of the four.

[18] The second source is the need to estimate  $u_s$  and  $v_s$ , which are not reported. We tried two approaches: setting their values to zero (our standard approach) and setting them equal to the wind speeds at 2 m in the SPARC archive. The Minneapolis example (Figure 1) shows that using the 2 m wind speeds as surface speeds yields  $z(\text{Ri}_{0.25}) = 1.471$  km, about 9% lower than setting surface speeds to zero. In general, although the resulting  $z(\text{Ri}_{0.25})$  are highly correlated ( $r = 0.91$ ), the plot in Figure 2b shows considerable scatter for  $z(\text{Ri}_{0.25}) < 2$  km, with uncertainties in this  $z(\text{Ri}_{0.25})$  range typically (median value)  $\sim 50$  to 150 m in the SPARC data and  $\sim 50$  to 200 m in the IGRA data. The larger uncertainties in the IGRA data may be related to its coarser vertical resolution and the need to interpolate the wind profile to obtain  $z(\text{Ri}_{0.25})$ , leading to larger uncertainties in 2 m wind speed estimates. For  $z(\text{Ri}_{0.25}) > 2$  km, absolute uncertainties are generally  $<100$  m and relative uncertainties  $<5\%$ .

[19] The third source of uncertainty (Figure 2c) is the interpolation of the Ri profile to locate the level at which  $\text{Ri} = 0.25$ , which generally is not a reported data level. We estimated this uncertainty as the vertical distance between the estimated (interpolated)  $z(\text{Ri}_{0.25})$  and the closest reported data level. Median and 75th percentile uncertainties are about 200 and 400 m, respectively, for most values of  $z(\text{Ri}_{0.25})$  in the IGRA data (but just 18 m in the example in Figure 1), and much smaller,  $<10$  m, in the higher-resolution SPARC data. For low  $z(\text{Ri}_{0.25})$  in the IGRA data, the interpolation obviously causes a large percentage uncertainty, but for  $z(\text{Ri}_{0.25}) > 1$  km, the uncertainty is generally well below 20%.

[20] Finally, we directly compare  $z(\text{Ri}_{0.25})$  from SPARC and IGRA soundings to quantify uncertainty associated with sounding vertical resolution. Recall that the mean number of levels below 500 hPa is 100 in the SPARC archive and 15 in the IGRA. In the Minneapolis case (Figure 1),  $z(\text{Ri}_{0.25})$  estimated using the SPARC and IGRA data are 1.615 and 1.579 km, respectively, a 2% difference. From the larger sample of SPARC and IGRA sounding pairs, for  $z(\text{Ri}_{0.25}) > 0.5$  km, we infer median absolute and relative uncertainties of about 50 m and 5%, respectively (Figure 2d). But for the shallowest  $z(\text{Ri}_{0.25})$ , uncertainties are more significant. Although highly correlated ( $r = 0.91$ ) there is much scatter for small  $z(\text{Ri}_{0.25})$  values, with 75th percentile relative uncertainties approaching 80% for  $z(\text{Ri}_{0.25}) < 0.5$  km.

[21] To summarize, many soundings, especially those taken at night or in the early morning hours, have  $z(\text{Ri}_{0.25}) < 1$  km as determined using the bulk Ri method. Relative uncertainties in that method can be large ( $>50\%$ ) for these low  $z(\text{Ri}_{0.25})$ , but they are much smaller (usually  $<20\%$ ) for  $z(\text{Ri}_{0.25}) > 1$  km. The choice of critical Ri does not introduce large uncertainty, but other methodological choices (including estimating of surface wind speeds and vertical interpolation of the Ri profile) as well as the native vertical resolution of the sounding data are larger uncertainty sources.

### 3.3. Climatological Statistics

[22] Using instantaneous  $z(\text{Ri}_{0.25})$  estimates from the radiosondes, ERA-Interim, and the two climate models, we computed 25-yr seasonal (DJF, MAM, etc.) 10th, 25th, 50th, 75th, and 90th percentile values for each station or grid point and for both regions studied, separately for 0000 and 1200 UTC. All  $z(\text{Ri}_{0.25})$  values are presented with reference to surface elevation, not sea level, to avoid conflating topographic variations with spatial variations in  $z(\text{Ri}_{0.25})$ . Model  $z(\text{Ri}_{0.25})$  values are with respect to model surface elevations. All climatological statistics, and instantaneous  $z(\text{Ri}_{0.25})$  values from radiosondes,

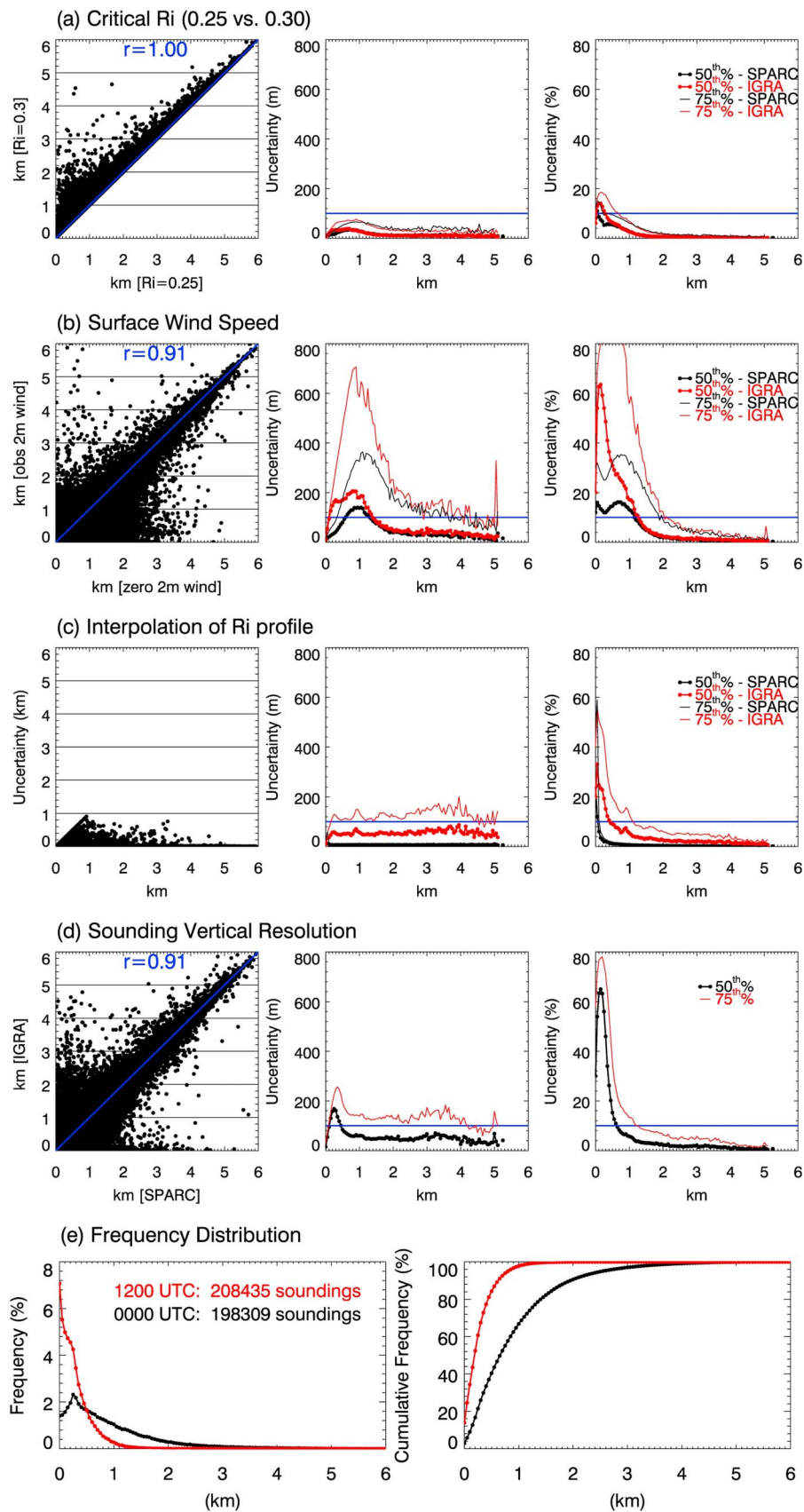
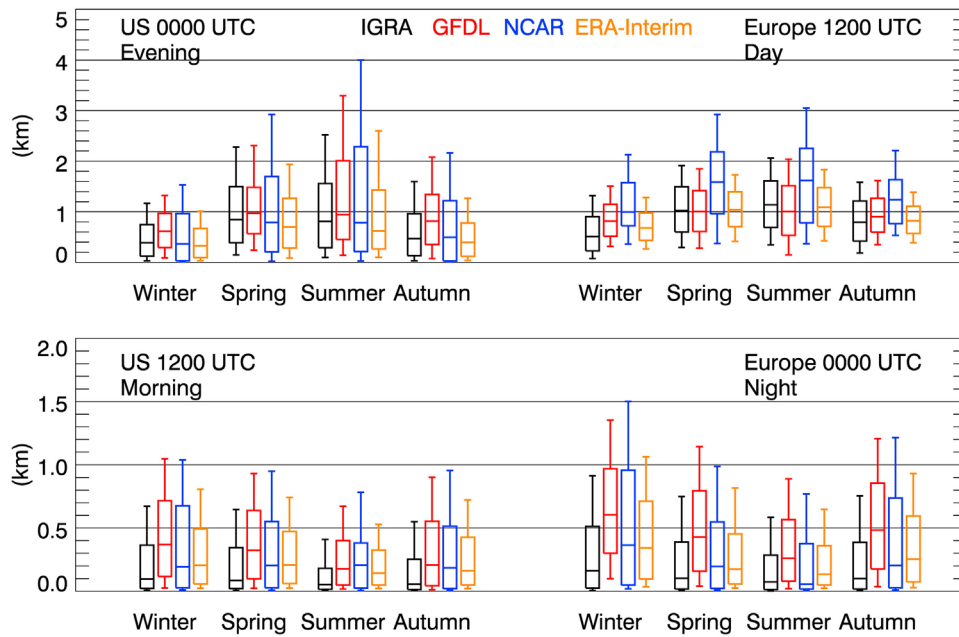


Figure 2



**Figure 3.** Box-and-whisker plots showing 10th, 25th, 50th, 75th, and 90th percentile values of instantaneous heights  $z(Ri_{0.25})$  during each season based on (top) daytime and (bottom) nighttime soundings over the U.S. and Europe, from the IGRA radiosonde data archive, the GFDL AM3 and NCAR CAM5 climate models, and the ERA-Interim. Each box-and-whisker plot is based on approximately 68,000 to 98,000 instantaneous values. Model and reanalysis results are for grid locations closest to radiosonde stations. Note the larger scale range for the plots of evening and daytime climatologies (top).

are provided as auxiliary material, in the hope that they might be useful in future studies.<sup>1</sup>

#### 4. Results

[23] This section presents the basic  $z(Ri_{0.25})$  climatologies from the four data sources for both continents, including seasonal and diurnal variations. Direct comparisons of climatological results from radiosonde observations with the ERA-Interim and with the NCAR CAM5 and GFDL AM3 models are made to elucidate biases. In a brief exploration of surface and upper-air influences on  $z(Ri_{0.25})$ , we present an analysis of annual cycle correlations between climatological

$z(Ri_{0.25})$  and three other variables: surface temperature and pressure, and 500 hPa height data.

##### 4.1. Climatological Patterns

[24] As a gross climatological overview, Figure 3 shows seasonal distributions of 0000 and 1200 UTC  $z(Ri_{0.25})$  over Europe and the U.S. from each of the four data sources, where the reanalysis and models have been sampled at grid points closest to the radiosonde locations. The radiosonde data indicate median daytime  $z(Ri_{0.25})$  values (Figure 3, top) are generally  $<1$  km over both continents, while median nighttime values (bottom) are  $<0.5$  km. Daytime values over Europe occasionally (90th percentile) reach 2 km in summer, and 2 km  $z(Ri_{0.25})$  are more often found daytime over the U.S. in both spring and summer. During daytime, spring and

<sup>1</sup>Auxiliary material data sets are available at <ftp://ftp.agu.org/apend/jd/2012jd018143/>. Other auxiliary material files are available in the HTML. doi:10.1029/2012JD018143.

**Figure 2.** (a) Comparison of heights,  $z(Ri_{0.25})$ , computed using 0.25 and 0.30 as critical bulk Richardson number in 406,644 soundings over the United States during the years 1998–2008 from the SPARC data archive and (correlation coefficient  $r$  (left); the 50th and 75th percentile values of the absolute uncertainty, expressed in meters (middle); and the associated relative uncertainty in  $z(Ri_{0.25})$ , expressed as a percentage of median  $z(Ri_{0.25})$  (right). The middle and right panels show uncertainties in 50 m  $z(Ri_{0.25})$  intervals and show uncertainties obtained from the matching soundings in the IGRA. (b) As in Figure 2a but comparison of heights computed using  $0 \text{ m s}^{-1}$  and the winds at 2m as surface wind speed. (c) Uncertainty in  $z(Ri_{0.25})$  due to vertical interpolation of the bulk Richardson number profile to locate the 0.25 critical value as a function of  $z(Ri_{0.25})$  (left) and resulting 50th and 75th percentile values of the associated absolute (middle) and relative (right) uncertainties, as in Figure 2a. (d) As in Figure 2a but comparison of heights computed from the higher resolution SPARC data archive and the lower resolution IGRA archive, using soundings for the same location and time (left) and resulting 50th and 75th percentile values of the associated absolute (middle) and relative (right) uncertainties, as a function of median  $z(Ri_{0.25})$  from the SPARC data, in 50 m intervals. (e) Frequency distribution (left) and cumulative frequency distribution (right) of heights at 0000 UTC (local daytime) and 1200 UTC (local nighttime) from the SPARC data archive.

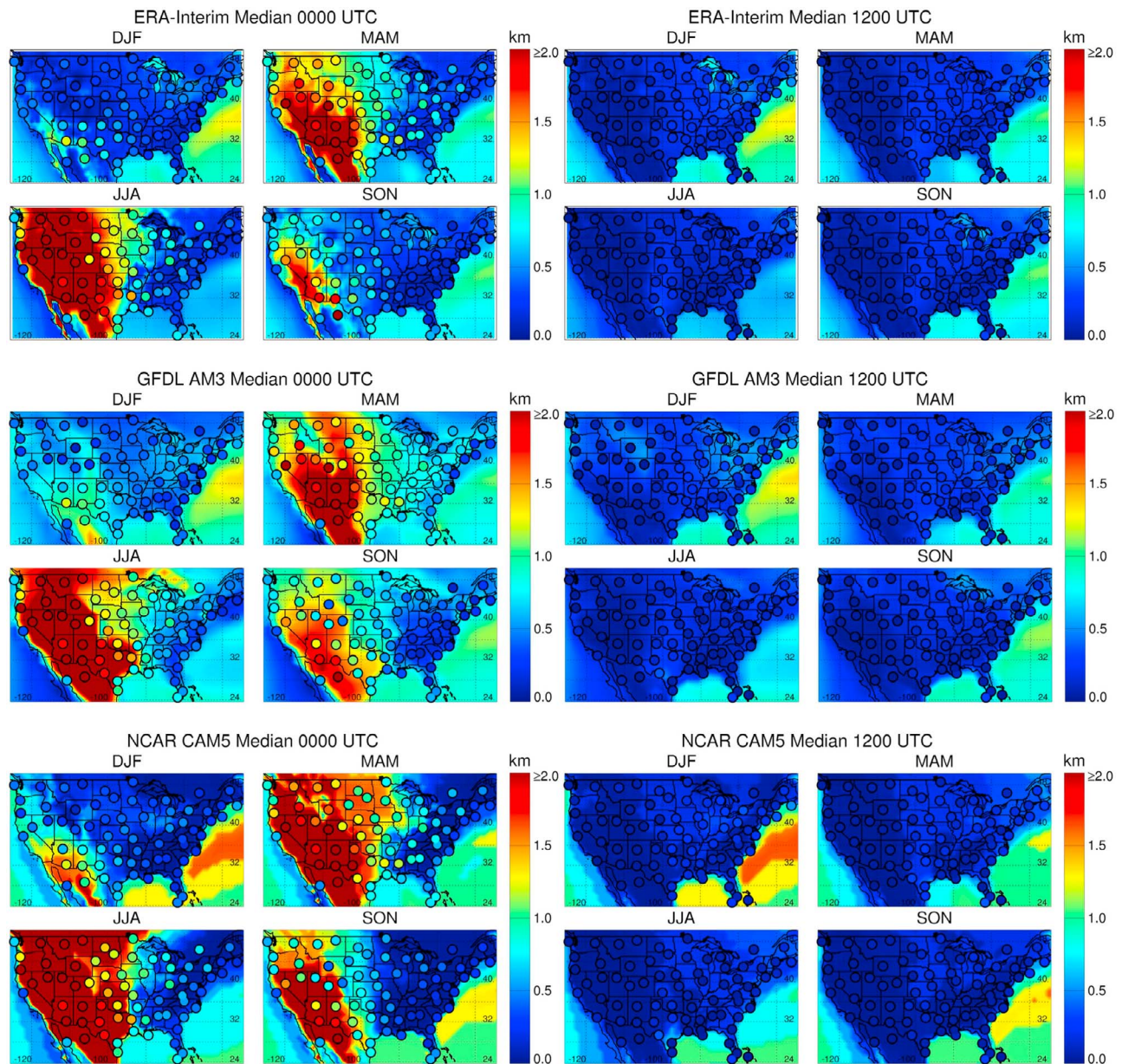


**Figure 4.** Map of median heights  $z(Ri_{0.25})$  over the U.S., for each season, from the IGRA radiosonde archive (dot symbols) and from (top) ERA-Interim, (middle) GFDL AM3 and (bottom) NCAR CAM5. Maps on left and right are for 0000 UTC and 1200 UTC, respectively.

summer  $z(Ri_{0.25})$  are higher than fall and winter, but the opposite seasonal patterns appear at night. Given the large percentage uncertainties associated with  $z(Ri_{0.25}) < 1$  km, the validity of this apparent nighttime pattern, which both regions exhibit, is questionable. A physical explanation for this pattern is the typically higher climatological wind speeds in winter than summer.

[25] Using the Wilcoxon rank sum and signed rank tests, we compared median values for each season, time of day, and data source. Given the very large ensembles, all medians are significantly different at the  $p = 0.05$  level or better, although the significance may be overestimated because the tests do not consider uncertainty estimates. Despite its incorporation of radiosonde data and matched spatial sampling, ERA-Interim yields  $z(Ri_{0.25})$  values consistently

higher than IGRA for nighttime. Both climate models also simulate higher nighttime  $z(Ri_{0.25})$  than IGRA, suggesting a general model difficulty in simulating shallow stable nighttime boundary layers. Daytime  $z(Ri_{0.25})$  are in better accord, although the NCAR model shows a high bias. The nighttime overestimate in NCAR CAM5 is more severe in winter than summer in Europe, whereas the GFDL AM3 overestimate is similar in all seasons. In daytime, on the other hand, median values from the GFDL AM3 simulations agree well with radiosonde observations from Europe, while the NCAR CAM5 simulates systematically higher  $z(Ri_{0.25})$ . Both models show consistently larger variance than the IGRA observations. Examining the tails of the distributions (25th and 75th percentile values), IGRA and the NCAR model are more likely to show very low  $z(Ri_{0.25})$  at night, and the

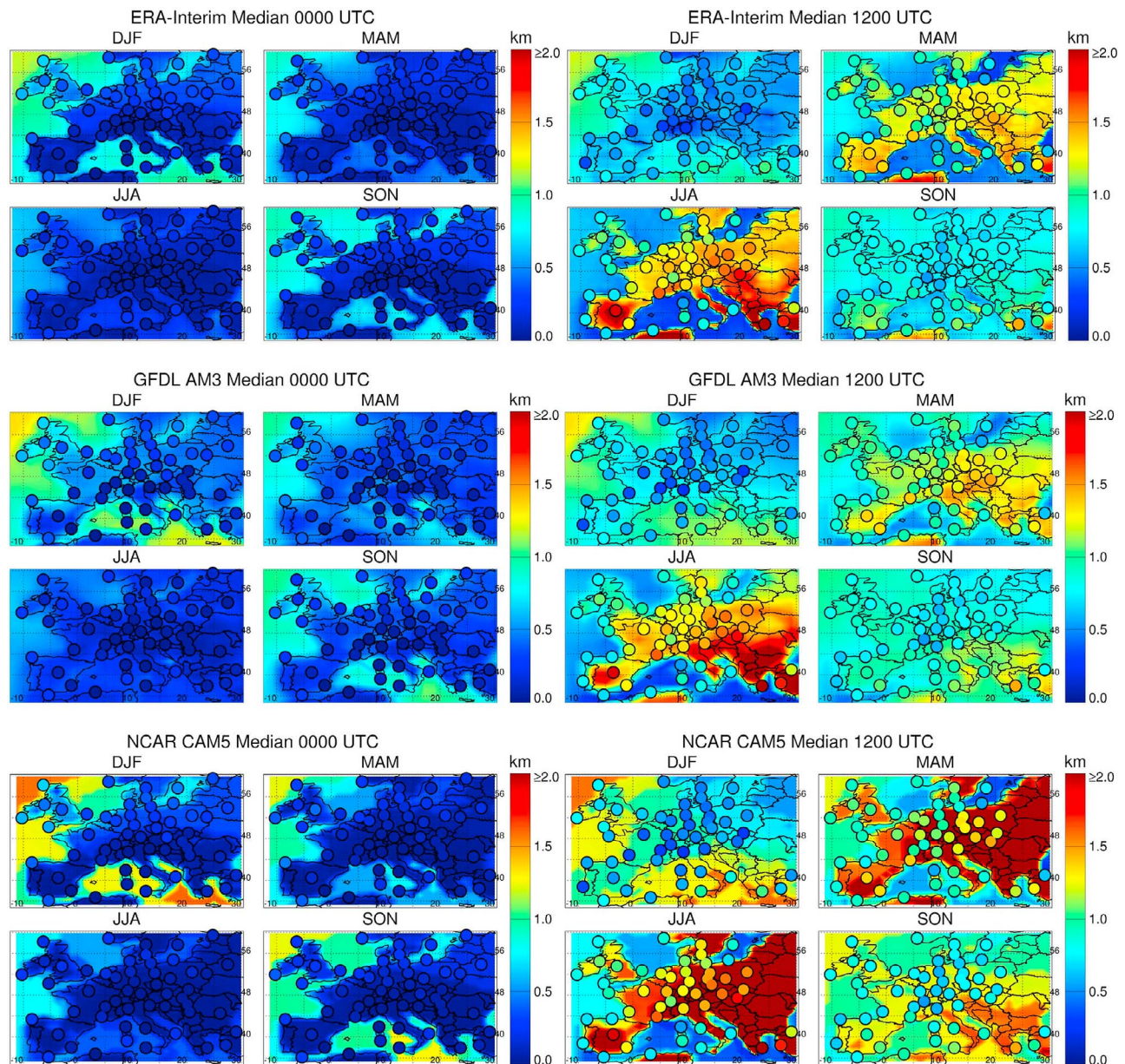


**Figure 5.** Map of median heights  $z(Ri_{0.25})$  over Europe, for each season, from the IGRA radiosonde archive (dot symbols) and from (top) ERA-Interim, (middle) GFDL AM3 and (bottom) NCAR CAM5. Maps on left and right are for 0000 UTC and 1200 UTC, respectively.

NCAR and GFDL models are more likely to show high values during daytime over the U.S. and at night in both regions.

#### 4.2. Seasonal Variations

[26] Figures 4 and 5 show maps of seasonal median  $z(Ri_{0.25})$  from each data source, for the U.S. and Europe, respectively. Corresponding maps of 10th and 90th percentile  $z(Ri_{0.25})$  values are provided in the auxiliary material (Figures S1, S2, S3, and S4). The maps superpose the IGRA results on the gridded ERA-Interim and climate model results, which are fully sampled within the domain, including ocean regions. The color scale was deliberately chosen to avoid emphasizing small differences for  $z(Ri_{0.25}) < 1$  km, consistent with our uncertainty analysis above.

[27] These maps reveal geographic variability not shown in the regional summaries of Figure 3. Over the U.S. (Figures 4, S1, and S2), there is strong 0000 UTC east-west  $z(Ri_{0.25})$  gradient, with higher  $z(Ri_{0.25})$  over the western states, particular during the warmer seasons. This gradient is captured by ERA-Interim and simulated by both climate models, which show the pattern as land-based. Because the region spans several time zones, the spatial variations observed at fixed observation times are conflated with diurnal variations, discussed in the next subsection. Because 0000 UTC is late afternoon in the western U.S. and early evening in the east, the high 0000 UTC  $z(Ri_{0.25})$  in the west are expected in association with afternoon convection, although other factors may also contribute to the east-west

gradient. Over ocean (where radiosonde data are not available), ERA-Interim and the climate models simulate  $z(\text{Ri}_{0.25})$  generally  $<1.5$  km (Figure S2), with less spatial and seasonal variability than over land. Similarly, the reanalysis and models show less difference between  $z(\text{Ri}_{0.25})$  at 0000 and 1200 UTC over ocean than over land. The reanalysis and models (particularly the NCAR model) also show higher oceanic  $z(\text{Ri}_{0.25})$  over the Gulf Stream, especially in winter, than over cooler regions of the North Atlantic. These high values of  $z(\text{Ri}_{0.25})$  are associated with high modeled wind shear, and so low bulk  $\text{Ri}$ , which may be exacerbated by our assumption of zero surface wind speed in evaluating  $\text{Ri}(z)$ . Given the lack of radiosonde observations over ocean, the validity of this feature is ambiguous.

[28] Land/sea differences are also apparent in Europe (Figures 5, S3, and S4). Like over the U.S., ERA-Interim and the climate models capture the seasonal and spatial variability of  $z(\text{Ri}_{0.25})$ . A notable difference in spatial variability over Europe is the north-south gradient in  $z(\text{Ri}_{0.25})$ , with higher values over southern Europe, in contrast with the east-west gradient over the U.S.

#### 4.3. Diurnal Variations

[29] Details of the complex diurnal changes in the structure of the planetary boundary layer [e.g., Stull, 1988] cannot possibly be captured in the twice-daily sampling of radiosonde observations. However, ERA-Interim data are available at eight times of day, and the two climate models provide output at four times daily, which allow us to make inferences about the amplitude and phase of diurnal variations and about the representativeness of the radiosonde observations. Figures 6 and 7 present seasonal variations in the diurnal cycle, derived from  $z(\text{Ri}_{0.25})$  for all days in 2000 at different times of day. See Figures S5 and S6 in the auxiliary material for maps, for the U.S. and Europe, respectively, of seasonal median  $z(\text{Ri}_{0.25})$  from ERA-Interim at 8 times of day. The close correspondence between the ERA-Interim and IGRA climatologies (Figures 4, 5, S1, S2, S3, and S4) gives confidence that the ERA-Interim representation of  $z(\text{Ri}_{0.25})$  at times intermediate to radiosonde observation times are not unreasonable.

[30] The seasonal median amplitude (hourly maximum minus hourly minimum  $z(\text{Ri}_{0.25})$ ) derived from ERA-Interim is higher in spring and summer in both regions (top halves of Figures 6 and 7), with largest amplitudes (up to 4 km) over the western U.S. In winter and fall, amplitudes in both regions are generally  $<1.5$  km. Phase peaks (hour of maximum  $z(\text{Ri}_{0.25})$ ) are in the afternoon. Comparison of ERA-Interim results based on eight and four times per day shows good agreement, suggesting that the climate model results, which are only available at four times daily, should capture the full diurnal cycle. Indeed, amplitude and phase estimates from the climate models generally resemble those from ERA-Interim. The most obvious differences are (1) the larger amplitudes over both the U.S. and Europe in NCAR CAM5 and (2) the differences in phase in the central U.S. in both GFDL AM3 and NCAR CAM5. On the other hand, the twice-daily radiosonde observations would not capture the full range of values for the U.S. (Figure S5), but fortuitously do capture the range over Europe (Figure S6).

[31] The eight-times-daily ERA-Interim results also help elucidate another aspect of the spatial variations in  $z(\text{Ri}_{0.25})$ .

If the high  $z(\text{Ri}_{0.25})$  over the western U.S. at 0000 UTC seen in Figure 4 were simply due to the peak of the diurnal cycle being better captured in this region than in the east, then we would expect the east-west gradient to be more pronounced at 0000 UTC than at other times in the ERA-Interim results (Figure S5), but this is not the case. Examination of the frequency distribution of  $z(\text{Ri}_{0.25})$  as a function of station elevation (not shown) revealed a clear tendency for higher  $z(\text{Ri}_{0.25})$  over high elevation stations in the U.S., with values exceeding 4 km at some higher elevation sites. In contrast, distributions over Europe do not show much dependence on station elevation. Whether this distinction is real or the result of the relative lack of high elevation European stations is unclear. (About 17 of the total 114 U.S. stations are at elevations  $>1.0$  km above mean sea level, but none of the 120 European stations is, because stations in mountainous regions of Europe tend to be located in valleys.) On the other hand, the drier climate of the U.S. and higher sun angle (associated with lower latitudes) may result in smaller latent and greater sensible heat flux at the surface, which should be associated with deeper convection and larger  $z(\text{Ri}_{0.25})$ .

#### 4.4. Comparison of Observations and Simulations

[32] Observed and modeled climatological  $z(\text{Ri}_{0.25})$  are compared using scatterplots of mean annual values at 0000 and 1200 UTC in Figure 8, with correlation coefficients ( $r$ ) for each model; comparable results for each season are presented in Figure S7. These data displays reveal both the fidelity of modeled patterns of spatial variation to the observations and potential systematic biases. For almost all comparisons, of both annual and seasonal data,  $0.5 < r < 0.9$ , indicating positive but not complete agreement in spatial patterns of variation. Over the U.S. (Figure 8 (left) and Figure S7 (top)), the clusters of points for 1200 UTC (night, early morning) with  $z(\text{Ri}_{0.25}) < 1$  km show lower correlations than the 0000 UTC (late afternoon, evening) values for both climate models and the reanalysis, and for each season except winter. This is perhaps because the spatial variations are weaker at 1200 UTC and in winter (Figure 4). Over the U.S., the climate models tend to overestimate and the reanalysis tends to underestimate  $z(\text{Ri}_{0.25})$ .

[33] These tendencies are not consistent between the U.S. and Europe. While the positive bias in the NCAR CAM5 results is similar in both regions, over Europe the positive bias in GFDL AM3 is limited to nighttime (0000 UTC) and the ERA-Interim bias is smaller than over the U.S. Furthermore, nighttime  $r$  values exceed daytime values for Europe, in contrast to the U.S. results. The poorer representation of daytime spatial variations (which are predominantly north-south) in Europe than in the U.S. (predominantly east-west) may be related to the issue of topography, addressed in the previous sub-section. The location of radiosonde stations in Europe at lower elevation than surrounding mountains, combined with the gross spatial resolution of the models, may compromise the comparison.

#### 4.5. Associations With Other Atmospheric Parameters

[34] Although the focus of this study is the climatology of  $z(\text{Ri}_{0.25})$ , this section presents a brief analysis of relationships between  $z(\text{Ri}_{0.25})$  climatology and that of three other standard climate variables—surface pressure, surface temperature, and 500 hPa geopotential height—in a preliminary

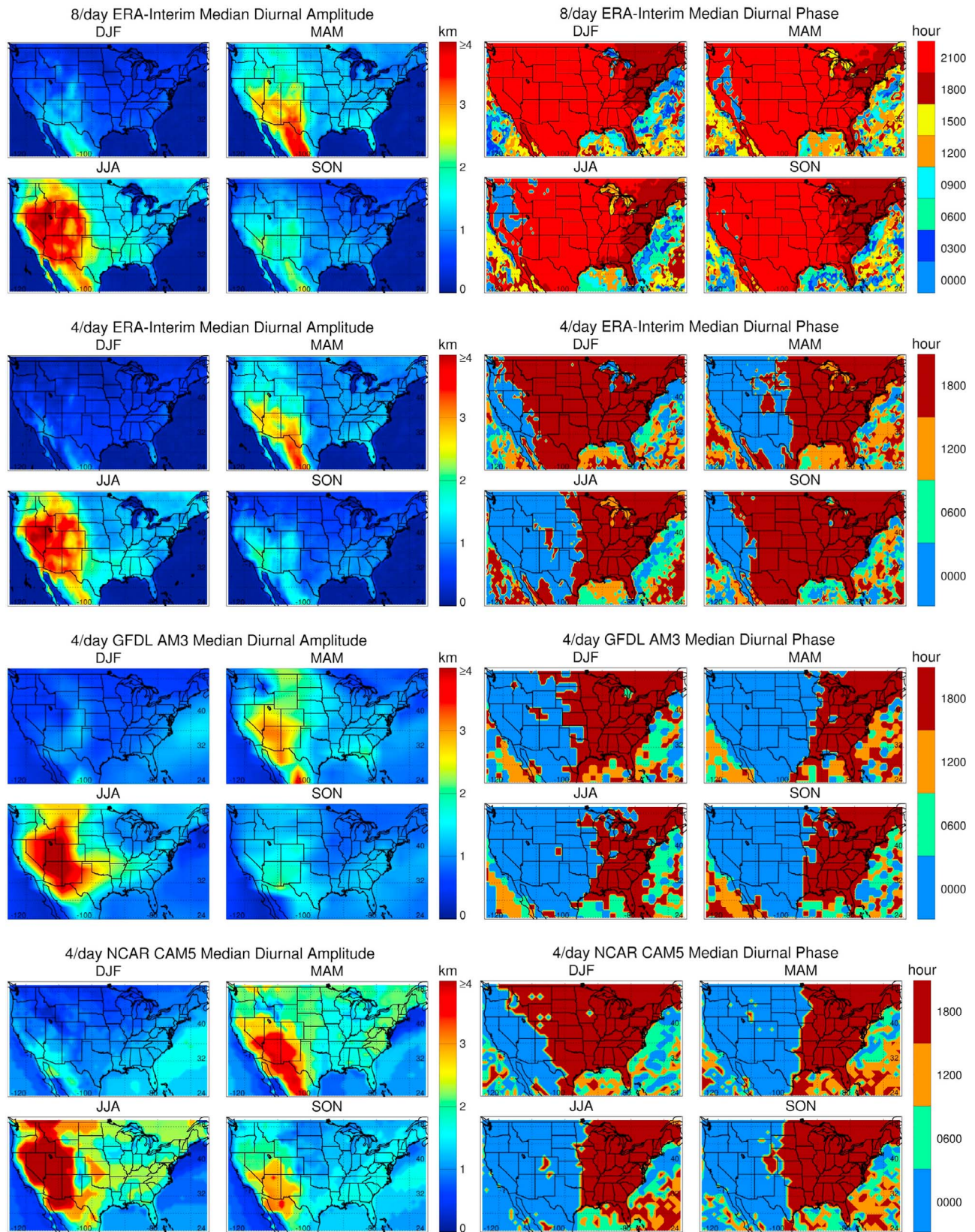


**Figure 6.** (left) Amplitude and (right) phase of the diurnal cycle of  $z(Ri_{0.25})$  over the U.S., for each season, based on: (top to bottom) eight-times-daily ERA-Interim data, and four-times-daily data from ERA Interim, GFDL AM3, and NCAR CAM5. Amplitudes are median values of daily maximum minus daily minimum, and phases are the hour of maximum  $z(Ri_{0.25})$ .

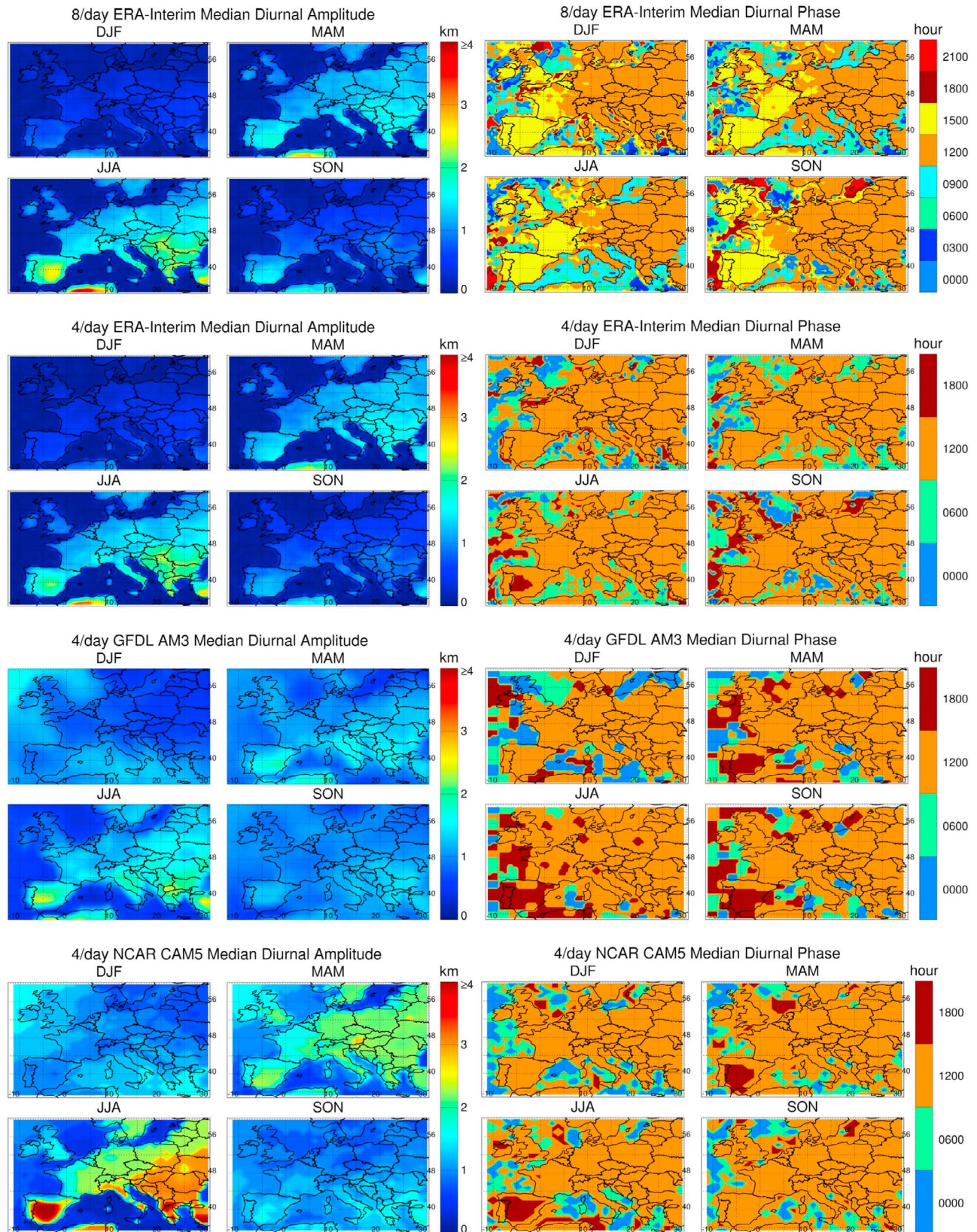
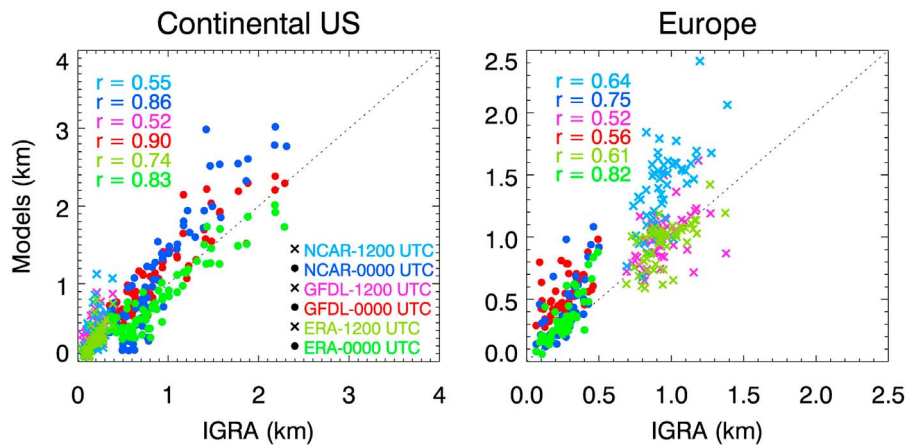


Figure 7. Same as Figure 6, but for Europe.



**Figure 8.** Scatterplot comparing climatological annual mean heights  $z(Ri_{0.25})$  based on radiosonde observations from IGRA to ERA-Interim (green), GFDL AM3 (red), and NCAR CAM5 (blue) values at the same locations, separated by observation time (dot and x for 0000 and 1200 UTC, respectively), and associated correlation coefficients, for the (left) U.S. and (right) Europe.

effort to discern patterns controlling seasonal variability. For example, Figure 9 compares the annual cycles of  $z(Ri_{0.25})$  with those of the three other variables at one station, Lindenberg, Germany. The strong annual cycle in daytime (1200 UTC)  $z(Ri_{0.25})$  is positively correlated with the daytime annual cycles of surface temperature ( $r = 0.85$ ) and 500 hPa height ( $r = 0.64$ ) all of which are higher in summer than winter, and anti-correlated with the annual cycle of surface pressure ( $r = -0.63$ ) which is lower in summer than winter. At night, the correlations are of opposite sign, because daytime and nighttime  $z(Ri_{0.25})$  values are anti-correlated (Figure 9).

[35] The 1981–2005 climatological monthly mean  $z(Ri_{0.25})$  values at Lindenberg in Figure 9 compare well with the 2001–2010 statistics obtained by *Beyrich and Leps* [2012, Figure 6] using a similar but not identical Ri formulation for estimating mixing height at a critical value of 0.20. We obtained slightly higher values for summertime, perhaps due to differences in the periods of record, sounding vertical resolution (higher in their study), and differences in Ri formulations and critical values. But the gross features of 0000 and 1200 UTC heights are in accord within the uncertainty estimates of both studies.

[36] Extending this analysis to the full set of radiosonde stations analyzed, Figure 10 shows correlations among these

variables over both regions for both 0000 and 1200 UTC. For daytime observations, the correlations at most stations in the U.S. and Europe are consistent with the results from Lindenberg. Specifically, the annual cycle of daytime  $z(Ri_{0.25})$  is positively correlated with surface temperature and 500 hPa geopotential height (all higher in summer than winter), and negatively correlated with surface pressure. This pattern does not hold for some stations along the Atlantic and Pacific coasts of the U.S. and for some stations along the Mediterranean and Atlantic coasts of Europe. The  $z(Ri_{0.25})$  at these coastal stations shows less annual variability than inland stations, probably due to the moderating influence of the ocean; therefore, correlations with other variables are weaker.

[37] Correlations for nighttime are generally of opposite sign than for daytime, due to the anti-correlation of daytime and nighttime  $z(Ri_{0.25})$ . Although nighttime  $z(Ri_{0.25})$  values are low and therefore more uncertain than daytime, the consistency of the nighttime annual variations, which show lower  $z(Ri_{0.25})$  in summer than winter, is a notable climatological feature.

[38] A similar correlation analysis (not shown) using surface humidity data was performed to determine if the spatial variations in  $z(Ri_{0.25})$ , particularly the strong east-west gradient in the U.S. in spring and summer, could be attributed

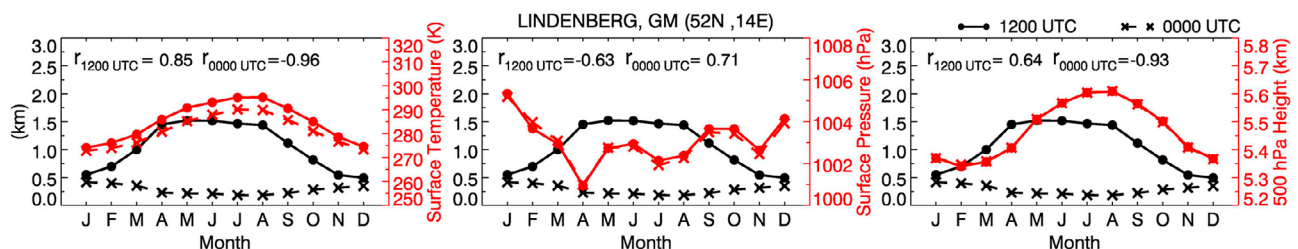


**Figure 9.** Climatological mean annual cycles of heights  $z(Ri_{0.25})$  and (left) surface temperature, (middle) surface pressure, and (right) 500 hPa height at Lindenberg, Germany ( $52^{\circ}\text{N}$ ,  $14^{\circ}\text{E}$ ) at 0000 UTC (x symbols) and 1200 UTC (dot symbols), and associated correlation coefficients. Surface pressure and 500 hPa height values at the two observation times are almost identical.

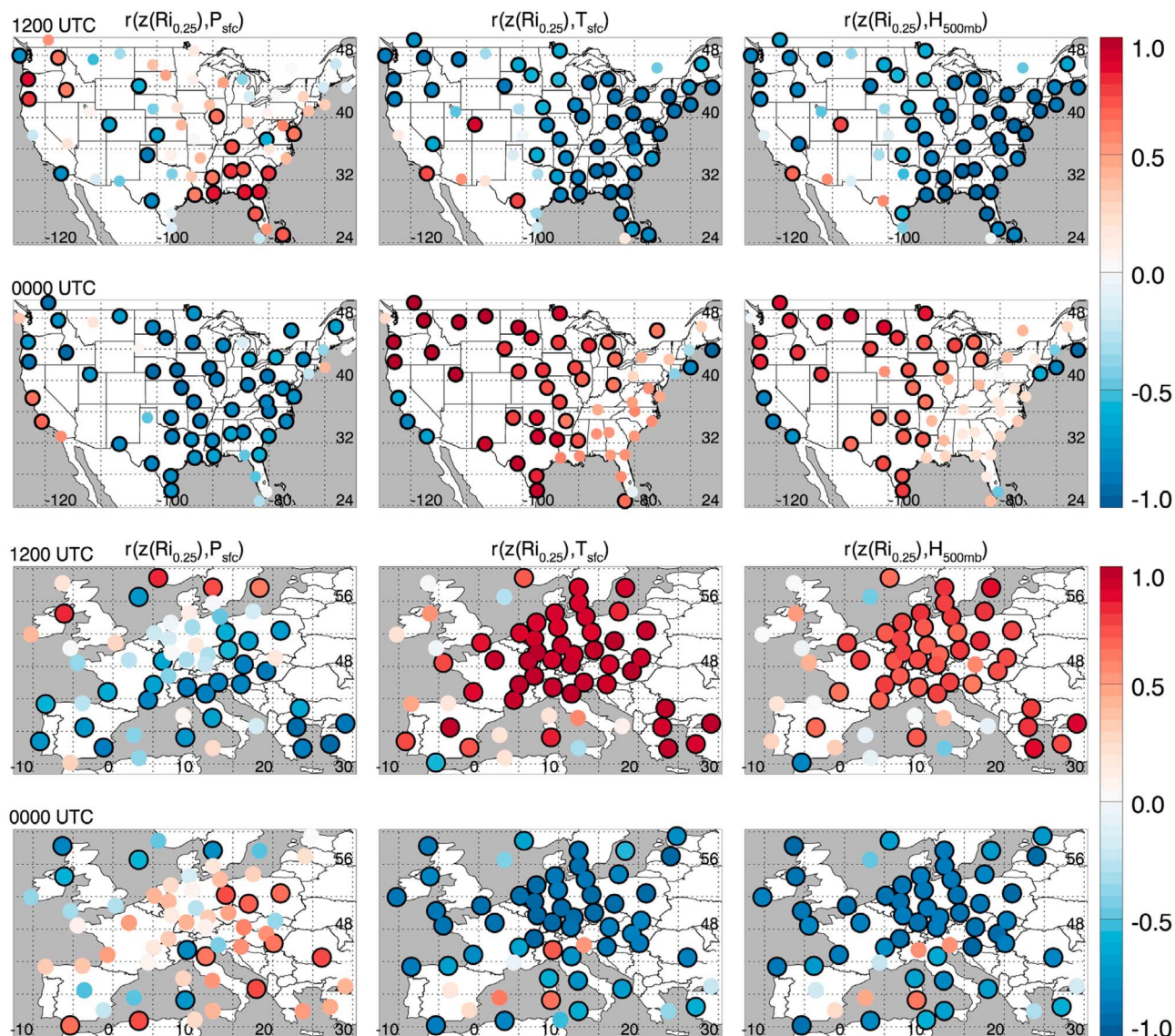


**Figure 10.** Correlations of mean annual cycles (12 monthly values) of heights  $z(Ri_{0.25})$  and (left) surface temperature, (middle) surface pressure, and (right) 500 hPa height at 1200 and 0000 UTC over the U.S. (top two panels) and Europe (bottom two panels) based on radiosonde data. Symbols outlined in black indicate values that are statistically significantly different from zero at the 95% confidence level.

to hydrologic factors, as suggested in Section 4.3. However, the strong seasonal and diurnal variations in relative humidity dominate spatial variations. Further analysis of the relation of  $z(Ri_{0.25})$  to moisture variables, including soil moisture, and of  $z(Ri_{0.25})$  variations on shorter (synoptic) time scales, in future studies may provide additional insight into the connections between boundary layer climatology and the hydrologic cycle.

## 5. Summary

[39] Analysis of the planetary boundary layer over Europe and the continental U.S. for the period 1981–2005 has revealed several noteworthy climatological features, despite methodological uncertainties and data limitations.

[40] Among the many methods in the literature for quantitatively characterizing boundary layer, or mixing, height,

an algorithm based on the bulk Richardson number proved to be most suitable for application to large radiosonde, reanalysis, and climate model data sets. Several factors contribute to uncertainties in these calculations, including the critical  $Ri$  value used (0.25 in this study), estimation of surface wind speeds, interpolation of the vertical profile of  $Ri$  to locate the critical value at  $z(Ri_{0.25})$ , and the vertical resolution of the atmospheric profile data. For  $z(Ri_{0.25}) < 1$  km uncertainties can exceed 50% of the estimated  $z(Ri_{0.25})$ , but for larger  $z(Ri_{0.25})$  the uncertainty is a much smaller percentage.

[41] Climatological  $z(Ri_{0.25})$  are generally  $< 1$  km during daytime and  $< 0.5$  km at night over both Europe and the U.S. During daytime, summertime  $z(Ri_{0.25})$  are greater (sometimes  $> 2$  km) than in wintertime. At night, the opposite is the case: winter values of  $z(Ri_{0.25})$  exceed summer values. Deeper boundary layers are found over the western U.S. than

other areas studied, which appears to be related to high topography.

[42] The climatological diurnal cycle of  $z(Ri_{0.25})$ , revealed in eight-times-daily ERA-Interim data, shows  $z(Ri_{0.25})$  reach maxima in the afternoon. Four-times-daily climate model output, and twice-daily radiosonde data, capture the amplitude of the diurnal cycle over Europe, but the radiosonde sampling does not capture peak values over the U.S. Amplitudes are typically higher in spring and summer (up to 4 km) than in fall and winter (about 1.5 km).

[43] The ERA-Interim (a reanalysis that assimilates atmospheric observations) and the NCAR CAM5 and GFDL AM3 (climate models that do not) all reproduce spatial, seasonal and diurnal patterns of PBL variability that resemble those derived from radiosonde data. Over the U.S., spatial variations are better simulated for daytime than nighttime conditions, and the climate models tend to overestimate and the reanalysis tends to underestimate  $z(Ri_{0.25})$ . The positive bias in the NCAR CAM5 results is similar in both regions, but over Europe the positive bias in GFDL AM3 is limited to nighttime and the ERA-Interim bias is smaller than over the U.S. Simulating shallow, stable boundary layers, which are common in midlatitude regions over land at night and in the winter, and at high latitudes [Zhang et al., 2011], is clearly a challenge for climate models [Medeiros et al., 2011] which may employ enhanced mixing at night over land [Cuxart et al., 2006].

[44] Observations show that, at most locations (but not at some coastal locations), seasonal variability of daytime  $z(Ri_{0.25})$  tends to be positively correlated with surface temperature and 500 hPa height, all of which are larger in summer than winter, and anticorrelated with surface pressure. Nighttime  $z(Ri_{0.25})$  is larger in winter than summer and so shows opposite correlation patterns.

[45] The data sets produced for this analysis are available as auxiliary material, and we encourage their use in further studies evaluating model boundary layer simulations. A study of the representation of  $z(Ri_{0.25})$  in models of the global carbon cycle is already underway.

[46] **Acknowledgments.** The bulk of this research was performed while Y. Zhang held a National Research Council Postdoctoral Research Associateship at NOAA's Air Resources Laboratory. We thank Sungsu Park (NCAR) for valuable discussions during the course of this research and Roland Draxler and Praveena Krishnan (NOAA Air Resources Laboratory), Bert Holtzlag (Wageningen University), and two anonymous reviewers for helpful and insightful comments on this manuscript. Brian Medeiros acknowledges support from the Office of Science, U.S. Department of Energy, Cooperative Agreement DE-FC02-97ER62402. NCAR is sponsored by the National Science Foundation.

## References

Angevine, W. M., A. B. White, and S. K. Avery (1994), Boundary layer depth and entrainment zone characterization with a boundary layer profiler, *Boundary Layer Meteorol.*, *68*, 375–385, doi:10.1007/BF00706797.

Beyrich, F. (1997), Mixing height estimation from sodar data: A critical discussion, *Atmos. Environ.*, *31*, 3941–3953, doi:10.1016/S1352-2310(97)00231-8.

Beyrich, F., and J.-P. Leps (2012), An operational mixing height data set from routine radiosounding at Lindenberg: Methodology, *Meteorol. Z.*, in press.

Bianco, L., and J. M. Wilczak (2002), Convective boundary layer depth: Improved measurement by Doppler radar wind profiler using fuzzy logic methods, *J. Atmos. Oceanic Technol.*, *19*, 1745–1758, doi:10.1175/1520-0426(2002)019<1745:CBLDIM>2.0.CO;2.

Cuxart, J., et al. (2006), Single-column model intercomparison for a stably stratified atmospheric boundary layer, *Boundary Layer Meteorol.*, *118*, 273–303, doi:10.1007/s10546-005-3780-1.

Dayan, U., R. Shenhav, and M. Graber (1988), The spatial and temporal behavior of the mixed layer in Israel, *J. Appl. Meteorol.*, *27*, 1382–1394, doi:10.1175/1520-0450(1988)027<1382:TSATBO>2.0.CO;2.

Dee, D. P., et al. (2011), The ERA-Interim reanalysis: Configuration and performance of the data assimilation system, *Q. J. R. Meteorol. Soc.*, *137*, 553–597, doi:10.1002/qj.828.

Donner, L. J., et al. (2011), The dynamical core, physical parameterizations, and basic simulation characteristics of the atmospheric component AM3 of the GFDL global coupled model CM3, *J. Clim.*, *24*, 3484–3519, doi:10.1175/2011JCLI3955.1.

Durre, I., and X. Yin (2008), Enhanced radiosonde data for studies of vertical structure, *Bull. Am. Meteorol. Soc.*, *89*, 1257–1262, doi:10.1175/2008BAMS2603.1.

European Center for Medium-Range Weather Forecasting (2006), Diagnostic boundary layer height, in *IFS Documentation CY31r1*, vol. 4, *Physical Processes*, pp. 45–46, Reading, U. K. [Available at <http://www.ecmwf.int/research/ifsdocs/CY31r1/index.html>.]

Eresmaa, N., A. Karppinen, S. M. Joffe, J. Räsänen, and H. Talvitie (2006), Mixing height determination by ceilometers, *Atmos. Chem. Phys.*, *6*, 1485–1493, doi:10.5194/acp-6-1485-2006.

Garratt, J. R. (1992), *The Atmospheric Boundary Layer*, 335 pp., Cambridge Univ. Press, Cambridge, U. K.

Guo, P., Y.-H. Kuo, S. V. Sokolovskii, and D. H. Lenschow (2011), Estimating atmospheric boundary layer depth using COSMIC radio occultation data, *J. Atmos. Sci.*, *68*, 1703–1713, doi:10.1175/2011JAS3612.1.

Hanna, S. R. (1969), The thickness of the planetary boundary layer, *Atmos. Environ.*, *3*, 519–536, doi:10.1016/0004-6981(69)90042-0.

Heffter, J. L. (1980), Air Resources Laboratories Atmospheric Transport and Dispersion Model, *NOAA Tech. Memo. ERL ARL-81*, 24 pp., NOAA, Silver Spring, Md. [Available at <http://www.arl.noaa.gov/reportsTechMemos.php>.]

Hennemuth, B., and A. Lammert (2006), Determination of the atmospheric boundary layer height from radiosonde and lidar backscatter, *Boundary Layer Meteorol.*, *120*, 181–200, doi:10.1007/s10546-005-9035-3.

Holtzlag, A. A. M., and B. A. Boville (1993), Local versus nonlocal boundary layer diffusion in a global climate model, *J. Clim.*, *6*, 1825–1842, doi:10.1175/1520-0442(1993)006<1825:LNVBLD>2.0.CO;2.

Holzworth, G. C. (1964), Estimates of mean maximum mixing depths in the contiguous United States, *Mon. Weather Rev.*, *92*, 235–242, doi:10.1175/1520-0493(1964)092<0235:EOMMMD>2.3.CO;2.

Holzworth, G. C. (1967), Mixing depths, wind speeds and air pollution potential for selected locations in the United States, *J. Appl. Meteorol.*, *6*, 1039–1044, doi:10.1175/1520-0450(1967)006<1039:MDWSAA>2.0.CO;2.

Joffe, S. M., M. Kangas, M. Heikinheimo, and S. A. Kitaigorodskii (2001), Variability of the stable and unstable atmospheric boundary layer height, *Boundary Layer Meteorol.*, *99*, 429–450, doi:10.1023/A:1018956525605.

Jordan, N. S., R. M. Hoff, and J. T. Bacmeister (2010), Validation of Goddard Earth Observing System-version 5 MERRA planetary boundary layer heights using CALIPSO, *J. Geophys. Res.*, *115*, D24218, doi:10.1029/2009JD013777.

Keder, J. (1999), Detection of inversions and mixing height by REMTECH PA2 sodar in comparison with collocated radiosonde measurements, *Meteorol. Atmos. Phys.*, *71*, 133–138, doi:10.1007/s007030050051.

Liu, S., and X.-Z. Liang (2010), Observed diurnal cycle climatology of planetary boundary layer height, *J. Clim.*, *23*, 5790–5809, doi:10.1175/2010JCLI3552.1.

Lokoshchenko, M. A. (2002), Long-term sodar observations in Moscow and a new approach to potential mixing determination by radiosonde data, *J. Atmos. Oceanic Technol.*, *19*, 1151–1162, doi:10.1175/1520-0426(2002)019<1151:LTSOIM>2.0.CO;2.

Marsik, F. J., K. W. Fischer, T. D. McDonald, and P. J. Sampson (1995), Comparison of methods for estimating mixing height used during the 1992 Atlanta Field Intensive, *J. Appl. Meteorol.*, *34*, 1802–1814, doi:10.1175/1520-0450(1995)034<1802:COMFEM>2.0.CO;2.

McGrath-Spangler, E. L., and S. Denning (2012), Estimates of North American summertime planetary boundary layer depths derived from space-borne lidar, *J. Geophys. Res.*, doi:10.1029/2012JD017615, in press.

Medeiros, B., C. Deser, R. A. Tomas, and J. E. Kay (2011), Arctic inversion strength in climate models, *J. Clim.*, *24*, 4733–4740, doi:10.1175/2011JCLI3968.1.

Neale, R. B., et al. (2010), Description of the NCAR community atmosphere model (CAM 5.0), *Tech. Rep. TN-486+STR*, 268 pp., Natl. Cent. for Atmos. Res., Boulder Colo. [Available at [http://www.cesm.ucar.edu/models/ccsm4.0/cam/docs/description/cam4\\_desc.pdf](http://www.cesm.ucar.edu/models/ccsm4.0/cam/docs/description/cam4_desc.pdf).]

Ratnam, M. V., and S. G. Basha (2010), A robust method to determine global distribution of atmospheric boundary layer top from COSMIC

- GPS RO measurements, *Atmos. Sci. Lett.*, *11*, 216–222, doi:10.1002/asl.277.
- Seibert, P., F. Beyrich, S. E. Gryning, S. Joffre, A. Rasmussen, and P. Tercier (2000), Review and intercomparison of operational methods for the determination of the mixing height, *Atmos. Environ.*, *34*, 1001–1027, doi:10.1016/S1352-2310(99)00349-0.
- Seidel, D. J., C. O. Ao, and K. Li (2010), Estimating climatological planetary boundary layer heights from radiosonde observations: Comparison of methods and uncertainty analysis, *J. Geophys. Res.*, *115*, D16113, doi:10.1029/2009JD013680.
- Stull, R. B. (1988), *An Introduction to Boundary Layer Meteorology*, 666 pp., Kluwer Acad., Dordrecht, Netherlands.
- Troen, I., and L. Mahrt (1986), A simple model of the atmospheric boundary layer: Sensitivity to surface evaporation, *Boundary Layer Meteorol.*, *37*, 129–148, doi:10.1007/BF00122760.
- Tucker, S. C., C. J. Senff, A. M. Weickmann, W. A. Brewer, R. M. Banta, S. P. Sandberg, D. C. Law, and R. M. Hardesty (2009), Doppler lidar estimation of mixing height using turbulence, shear, and aerosol profiles, *J. Atmos. Oceanic Technol.*, *26*, 673–688, doi:10.1175/2008JTECHA1157.1.
- van der Kamp, D., and I. McKendry (2010), Diurnal and seasonal trends in convective mixed layer heights estimated from two years of continuous ceilometer observations in Vancouver BC, *Boundary Layer Meteorol.*, *137*, 459–475, doi:10.1007/s10546-010-9535-7.
- Vogelezang, D. H. P., and A. A. M. Holtslag (1996), Evaluation and model impacts of alternative boundary-layer height formulation, *Boundary Layer Meteorol.*, *81*, 245–269, doi:10.1007/BF02430331.
- Wang, L., and M. A. Geller (2003), Morphology of gravity-wave energy as observed from 4 years (1998–2001) of high vertical resolution U.S. radiosonde data, *J. Geophys. Res.*, *108*(D16), 4489, doi:10.1029/2002JD002786.
- Yamada, T. (1979), PBL similarity profiles determined from a level-2 turbulence-closure model, *Boundary Layer Meteorol.*, *17*, 333–351, doi:10.1007/BF00117923.
- Zhang, Y., D. J. Seidel, J.-C. Golaz, C. Deser, and R. A. Tomas (2011), Climatological characteristics of Arctic and Antarctic surface-based inversions, *J. Clim.*, *24*, 5167–5186, doi:10.1175/2011JCLI4004.1.
- Zilitinkevich, S., and A. Baklanov (2002), Calculation of the height of the stable boundary layer in practical applications, *Boundary Layer Meteorol.*, *105*, 389–409, doi:10.1023/A:1020376832738.